ble for a wide number of bimetallic systems, opening up new perspectives for studying and understanding electrochemical reactions on bimetallic surfaces on a microscopic scale and establishing an atomic-scale mechanism of electrocatalytic reactions.

References and Notes

1. M. Watanabe, S. Motoo, *J. Electroanal. Chem.* **60**, 275 (1975).
2. W. F. Lin *et al.*, *J. Phys. Chem. B* **103**, 6968 (1999).
3. C. T. Campbell, in *Handbook of Heterogeneous Catalysis*, G. Ertl, H. Knözinger, J. Weitkamp, Eds. (Wiley, Weinheim, 1997), vol. 2, p. 814.
4. P. N. Ross, in *Electrocatalysis*, J. Lipkowski, P. N. Ross, Eds. (Wiley, New York, 1998), p. 43.
5. Also for gas-phase catalysis a direct, quantitative evaluation of ensemble/ligand effects had not been possible so far for the same reason, i.e., insufficient information on the exact distribution of surface atoms.
6. R. C. Newman, K. Sieradzki, *Science* **263**, 1708 (1994).
7. H. A. Gasteiger, N. Markovic, P. N. Ross, *Catal. Lett.* **36**, 1 (1996).
8. PdAu alloy films were electrodeposited at 0.3 $V_{Ag/AgCl}$ on Au(111) rotating disk electrodes (2000 rpm) from 0.1 M H_2SO_4 solution (suprapure), containing $x \cdot 10^{-6}$ M K_2PdCl_4 and $y \cdot 10^{-6}$ M $KAuCl_4$ (pro analysis grade) with $x + y = 3.5$ and the ratio x:y equal to 1:9 ($Pd_{07}Au_{93}$), 1:4 ($Pd_{15}Au_{85}$), 3:7 ($Pd_{22}Au_{78}$), 1:1 ($Pd_{37}Au_{63}$), and 7:3 ($Pd_{52}Au_{48}$). After rinsing with Milli-Q water the samples were transferred into the cell of the (home-built) STM, into the IR spectrometer cell, or into a separate cell for electrochemical measurements (hanging meniscus geometry, de-aerated with 6.0 Ar), where they were studied in 0.1 M H_2SO_4 solution. CO adsorption was performed at −0.15 $V_{Ag/AgCl}$ by saturating the solution for 10 min with 4.7 CO, followed by 30 min of 6.0 Ar purging.
9. M. Baldauf, D. M. Kolb, *Electrochim. Acta* **38**, 2145 (1993).
10. L. A. Kibler, M. Kleinert, R. Randler, D. M. Kolb, *Surf. Sci.* **443**, 19 (1999).
11. H. Naohara, S. Ye, K. Uosaki, *J. Phys. Chem. B* **102**, 4366 (1998).
12. F. Maroun, F. Ozanam, O. M. Magnussen, R. J. Behm, unpublished data.
13. C. Nagl, O. Haller, E. Platzgummer, M. Schmid, P. Varga, *Surf. Sci.* **321**, 237 (1994).
14. A. K. Schmid, J. C. Hamilton, M. C. Bartelt, R. Q. Hwang, *Phys. Rev. Lett.* **77**, 2977 (1996).
15. B. Sadigh *et al.*, *Phys. Rev. Lett.* **83**, 1379 (1999).
16. B. Gleich, M. Ruff, R. J. Behm, *Surf. Sci.* **386**, 48 (1997).
17. L. A. Kibler, M. Kleinert, D. M. Kolb, *Surf. Sci.* **461**, 155 (2000).
18. M. P. Green, K. J. Hanson, R. Carr, I. Lindau, *J. Electrochem. Soc.* **137**, 3493 (1990).
19. In a single case only, for a $(\sqrt{3} \times \sqrt{3})$ R30° superstructure formed upon Tl deposition on Ag(111), in situ STM observations were associated with an alloy formation, but without clear identification of the two metal components (*30*).
20. F. R. de Boer, R. Boom, W. C. M. Mattens, A. R. Miedema, A. K. Niessen, *Cohesion in Metals: Transition Metal Alloys* (North-Holland, Amsterdam, 1988).
21. M. F. Sykes, M. Glen, *J. Phys. A.* **9**, 87 (1976).
22. A similar analysis of alloys with higher Pd content, where larger Pd multimers also contribute substantially, was omitted, because the most important aspects in the chemistry of these surfaces can be understood based on the analysis of low-Pd content data.
23. S. Zou, R. Gómez, M. J. Weaver, *J. Electroanal. Chem.* **474**, 155 (1999).
24. L.-J. Wan *et al.*, *J. Electroanal. Chem.* **484**, 189 (2000).
25. N. Hoshi, K. Kagaya, Y. Hori, *J. Electroanal. Chem.* **485**, 55 (2000).
26. N. M. Markovic, C. Lucas, V. Climent, V. Stamenkovic, P. N. Ross, *Surf. Sci.* **465**, 103 (2000).
27. B. Álvarez, V. Climent, A. Rodes, J. M. Feliu, *J. Electroanal. Chem.* **497**, 125 (2001).
28. Y. L. Lam, J. Criado, M. Boudard, *J. Chim.* **1**, 461 (1977).
29. Additional contributions to the current come from double-layer charging and sulfate adsorption. The former was corrected by approximating the double-layer capacity of Pd_xAu_{1-x} with a weighted average of those of bare Au(111) and a three-ML Pd film on Au(111), i.e., assuming $C_{PdAu} = x \cdot C_{Pd} + (1 - x) \cdot C_{Au}$. The amount of sulfate desorption/adsorption, which occurs on Pd(111) parallel to H adsorption/desorption, cannot easily be assessed for the alloy and considerably contributes to the experimental error in θ_H. Assuming that local sulfate coverage and adsorption charge are similar on Pd ensembles and on Pd(111) [$\theta_{SO_4^{2-},max} = 0.2$ ML, $q_{SO_4^{2-},max} = 90$ μC cm^{-2} (*27*)], the H coverage will be at most 30% less than that where the contribution of sulfate is neglected, an error that does not affect the conclusions on the critical Pd ensemble size.
30. D. Carnal, P. I. Oden, U. Müller, E. Schmidt, H. Siegenthaler, *Electrochim. Acta* **40**, 1223 (1995).

31. We gratefully acknowledge fellowships from "Délégation Générale pour l'Armement" of France and the Alexander von Humboldt foundation as well as financial support by the CNRS and by the Deutsche Forschungsgemeinschaft (BE 1201/6-2). We also thank P. Liu and J. K. Nørskov (Technical University of Denmark) for discussions.

18 April 2001; accepted 31 July 2001

Mantle Flow Beneath a Continental Strike-Slip Fault: Postseismic Deformation After the 1999 Hector Mine Earthquake

Fred F. Pollitz,* Chuck Wicks, Wayne Thatcher

Two recent large earthquakes in the Mojave Desert, California—the magnitude 7.3 1992 Landers and magnitude 7.1 1999 Hector Mine earthquakes—have each been followed by elevated crustal strain rates over periods of months and years. Geodetic data collected after the Hector Mine earthquake exhibit a temporally decaying horizontal velocity field and a quadrant uplift pattern opposite to that expected for localized shear beneath the earthquake rupture. We interpret the origin of this accelerated crustal deformation to be vigorous flow in the upper mantle in response to the stress changes generated by the earthquake. Our results suggest that transient flow in the upper mantle is a fundamental component of the earthquake cycle and that the lower crust is a coherent stress guide coupling the upper crust with the upper mantle.

Mineral physics dictates that beneath the continental upper crust, the temperature of rocks is sufficiently high that the underlying lower crust and mantle flow through various solid state creep mechanisms (*1–4*). The mechanics of stress evolution in Earth's continental crust remain to be resolved. Central issues are whether strain accumulation in continental shear zones is driven by thick bounding blocks or by localized shear beneath the faults, whether the lower crust flows more or less readily than the upper mantle, and whether faults penetrate to depths substantially greater than seismogenic depths (~15 km in the western United States). Postseismic readjustment of the crust after the 16 October 1999 Hector Mine earthquake (Fig. 1A) carries large signals from potentially deep flow processes, and observations of this readjustment can characterize its mechanism, as well as yield clues to the rheology of the lower crust and upper mantle.

We analyzed synthetic aperture radar (InSAR) and Global Positioning System (GPS) data collected during the first 9 months after the Hector Mine earthquake (Figs. 1, B, C, and E, and 2, A and B) to determine the postseismic surface velocity field. The Hector Mine earthquake involved about 2 m of right-lateral slip along a 40- to 50-km-long fault (*5*, *6*), and the event altered the rate and pattern of regional aseismic crustal deformation. The InSAR data recorded range change, the change in distance between Earth's surface and an orbiting satellite (*7*, *8*), during the 9-month postseismic epoch. The measured range change is attributed primarily to vertical movement of Earth's surface but is also affected by horizontal movements. A total of three image pairs, covering three different time periods over the first 9 months of the postseismic epoch, were used to construct the interferograms (Fig. 1, B, C, and E) (*9*). GPS data carry independent information about horizontal and vertical movements, but we restrict our analysis to the horizontal velocity field changes because of their relatively small errors.

Postseismic InSAR deformation exhibits local, near-fault motions, but here we focus on the long-wavelength signal (>~30 km), which exhibits a quadrant pattern. This pattern is similar for the three depicted time periods, as shown by

U.S. Geological Survey, 345 Middlefield Road, MS 977, Menlo Park, CA 94025, USA.

*To whom correspondence should be addressed. E-mail: fpollitz@usgs.gov

the interferograms and a fault-parallel profile (Fig. 3). The two independent longer interferograms (Figs. 1, C and E, and 3, B and C), which have no scenes in common, show the strongest similarities, including range decrease lobes (predominantly uplift) centered on (35.1°N, −116.0°E) and (34.3°N, −116.3°E) and a range change increase lobe (subsidence) near (34.7°N, −116.8°E). The short, 1-month-long interferogram (Figs. 1B and 3A) has lower amplitudes, but it shares the same long-wavelength behavior west of the Hector Mine fault. Features near the eastern edge of the interferograms represent elevation-dependent noise (Fig. 1, B, C, and E). If interpreted in terms of vertical motions, the range change pattern would indicate ~15 to 20 mm of uplift in the north and south quadrants and a similar amount of subsidence in the east and west quadrants. The InSAR and GPS data sets contain about 30 to 40 mm/year of velocity signals; the horizontal postseismic velocity is about four times higher than the cumulative pre-1992 velocity across all of the central Mojave faults (*10*, *11*). These features suggest a deep transient source for the postseismic deformation, and we consider two possible processes: (i) afterslip on discrete planes underlying the Hector Mine seismogenic ruptures and (ii) broadly distributed viscoelastic flow in the ductile lower crust and upper mantle (*12*). For purposes of modeling, we use the 20 October 1999 to 21 June 2000 time period for the InSAR and GPS data sets.

In our modeling approach, we consider three-dimensional displacement at point $\hat{\mathbf{r}}$ on Earth's surface between times t_1 and t_2 as

$$\mathbf{u}(\hat{\mathbf{r}};t_1,t_2)=[\mathbf{u}_{\text{def}}(\mathbf{r};t_2)-\mathbf{u}_{\text{def}}(\mathbf{r};t_1)] + \mathbf{v}_{\text{load}}(\hat{\mathbf{r}})(t_2-t_1)+\mathbf{u}_{\text{trans}}(\hat{\mathbf{r}})+\mathbf{u}_{\text{tilt}}(\hat{\mathbf{r}}) \quad (1)$$

where $\mathbf{u}_{\text{def}}$ is afterslip-model or viscoelastic-model deformation, $\mathbf{v}_{\text{load}}$ is the secular tectonic-loading velocity field, $\mathbf{u}_{\text{trans}}$ represents uniform three-dimensional translation of all surface points, and $\mathbf{u}_{\text{tilt}}$ represents tilt about a horizontal axis. The corresponding range change is given by $\mathbf{u}(\hat{\mathbf{r}};t_1, t_2)\cdot\hat{\mathbf{l}}$, where $\hat{\mathbf{l}}$ is the unit vector in the range direction.

The secular tectonic velocity field is constructed from a uniform engineering shear strain rate of 0.1 μstrain/year resolved on a N40°W-trending vertical plane, approximately the pre-Landers horizontal deformation field (*11*). The $\mathbf{u}_{\text{trans}}$ and $\mathbf{u}_{\text{tilt}}$ terms are determined by inversion of the data simultaneously with the deformation processes and remove the influence of errors in the reference frame of the data sets for that particular time interval. These arise mainly from imperfect knowledge of satellite orbits in the InSAR data as well as the motion of the Hector Mine epicentral area with respect to the regional International Terrestrial Reference Frame (ITRF97). Independent processing of the GPS data within the regional ITRF97 and rigid North America reference frames, respectively, shows that the former moves about 12 mm/year toward N10°E with respect to the latter. This differs somewhat from

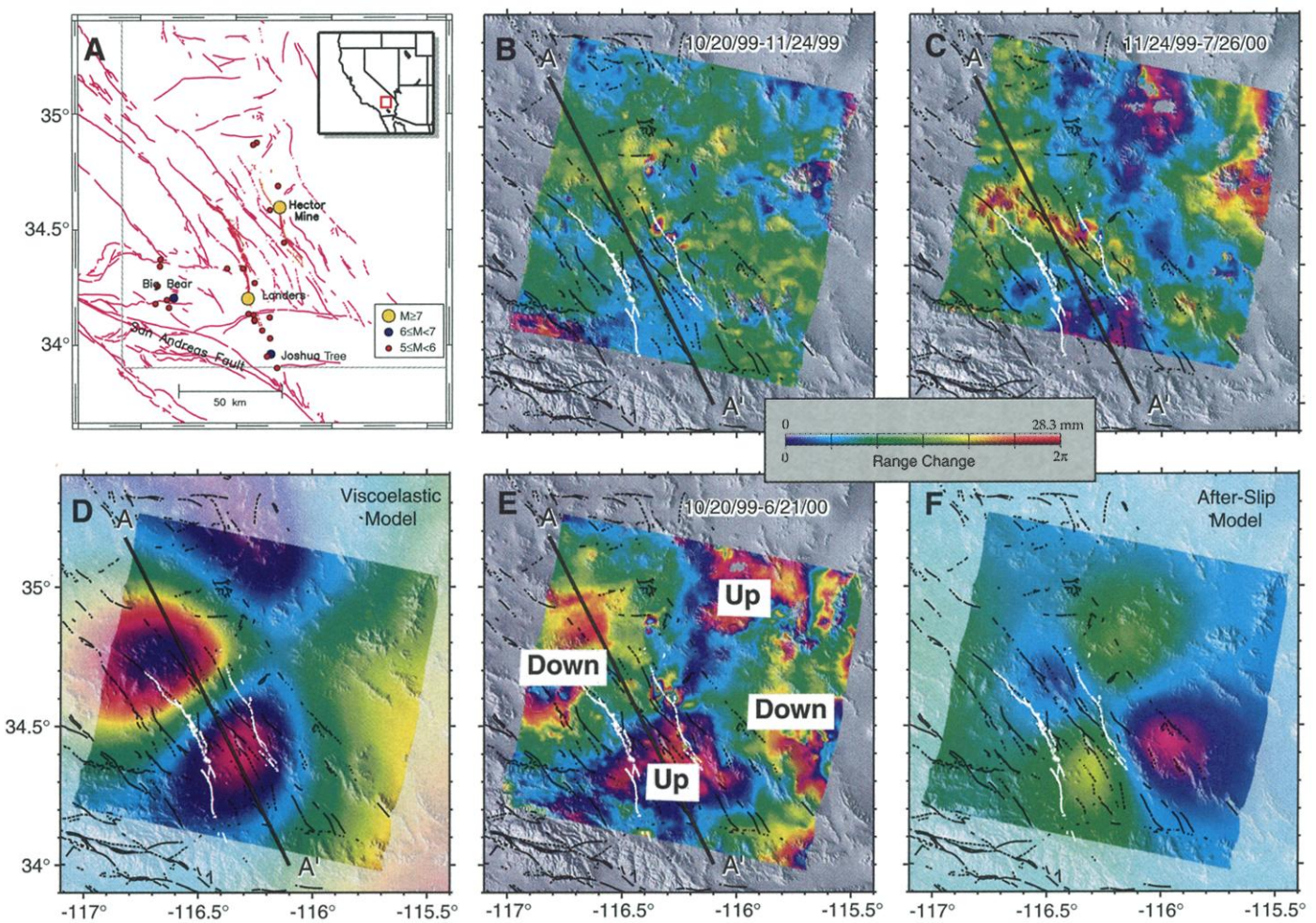

Fig. 1. (**A**) Background map indicating the most substantial earthquakes in the Mojave Desert from 1992 to 2000. Gray lines delineate the area covered in the following subplots. (**B**, **C**, and **E**) Observed ascending orbit wrapped interferograms during various time periods after the Hector Mine earthquake (*9*). One color cycle represents 28 mm of ground displacement away from the satellite with look and track angles (*8*) of 23° and S77°E, respectively. (**D** and **F**) Predictions of range change according to the viscoelastic and afterslip models, respectively, for the time period 20 October 1999 to 21 June 2000. The variance reduction of these models with respect to the observed interferogram in (E) is 67% and −56%, respectively. Peak-to-peak signal is generally slightly greater than 28 mm and is almost entirely captured with one color cycle.

the ~8 mm/year toward N40°W motion of the central Mojave Desert with respect to stable North America determined from very long baseline interferometry data (*13*), and this difference is essentially absorbed by $\mathbf{u}_{trans}$. The deformation component $\mathbf{u}_{def}(\mathbf{r}; t)$ is calculated from appropriate dislocations imposed within the upper portion of a spherically layered viscoelastic Earth model, consisting of an elastic upper crust underlain by a viscoelastic lower crust and upper mantle of viscosity η_c and η_m, respectively (*14*).

Models are evaluated in terms of the L_1 or L_2 norm misfit, weighted by the data errors, with respect to the null model or a particular physical model (in the L_2 case, the initial and residual variance, respectively). In particular, variance reduction is defined as 100% × (1 − residual variance/initial variance).

To estimate an afterslip model, we invert in a least squares sense the GPS data set alone for distributed right-lateral afterslip at 16- to 36-km depth on hypothetical vertical planes beneath two representative Hector Mine rupture planes (*15*) (red segments of Fig. 2A) yielding ~100 mm/year of afterslip on these planes. Calculated horizontal velocity is in reasonable agreement with observed velocity (Fig. 2A), but the calculated range change (Fig. 1F) is anticorrelated with the observed range change (Fig. 1E), leading to a poor fit (variance reduction = −55%). This modeling does not include any contribution of post-Landers relaxation, but its inclusion can account for only a small fraction of the observed range change. The peak-to-peak variation in range change rate over the area from late 1992 to early 1996 was about 15 mm/year (*16*). Furthermore, the post-Landers range change rate based on a viscoelastic coupling model (*16*), projected forward to the early post–Hector Mine epoch, is only 6 mm/year, so that any contribution of post-Landers relaxation beyond the 1999 Hector Mine event will probably be much smaller than the ~40 mm/year signal in the post–Hector Mine interferograms. The InSAR mismatch cannot be remedied with any distribution of deep afterslip beneath the Hector Mine rupture along a right-lateral fault, involving either deeper or more laterally extensive dislocation surfaces, nor with inclusion of post-Landers relaxation effects, and for this reason joint inversion of the InSAR and GPS data sets cannot yield a physically plausible afterslip distribution.

A model of postseismic relaxation of the lower crust and upper mantle successfully explains these data. A grid search of residual misfit of the separate InSAR and GPS data sets with respect to the viscoelastic deformation model is obtained as a function of η_c and η_m (Fig. 4). The misfit patterns show that mantle viscosity is between ~3 and 8×10^{17} Pa s and that $\eta_c \gg \eta_m$; i.e., the mantle is

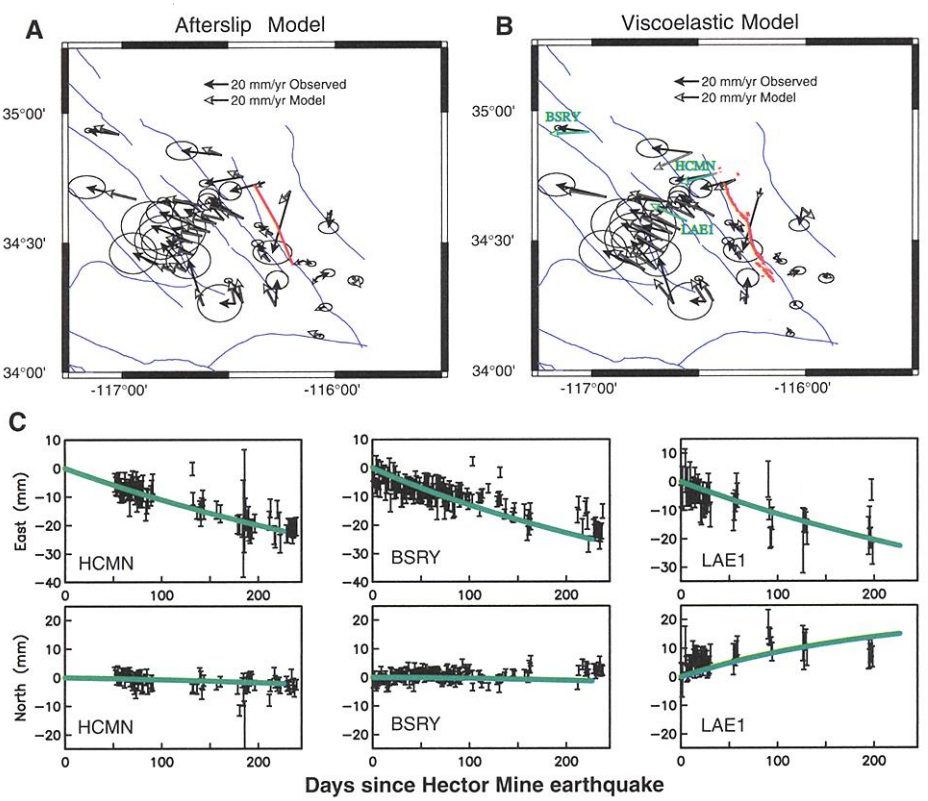

Fig. 2. Observed horizontal velocity field with respect to a regional ITRF97 reference frame and 95% confidence regions compiled from 29 continuous and campaign GPS stations (*32*). Superimposed are the predictions of the (**A**) afterslip and (**B**) viscoelastic models. Two red line segments in (A) denote traces of vertical afterslip planes used in the afterslip modeling. (**C**) GPS time series with standard errors at three sites labeled by green arrows in (B) with corresponding cumulative displacement (green line) according to the viscoelastic model.

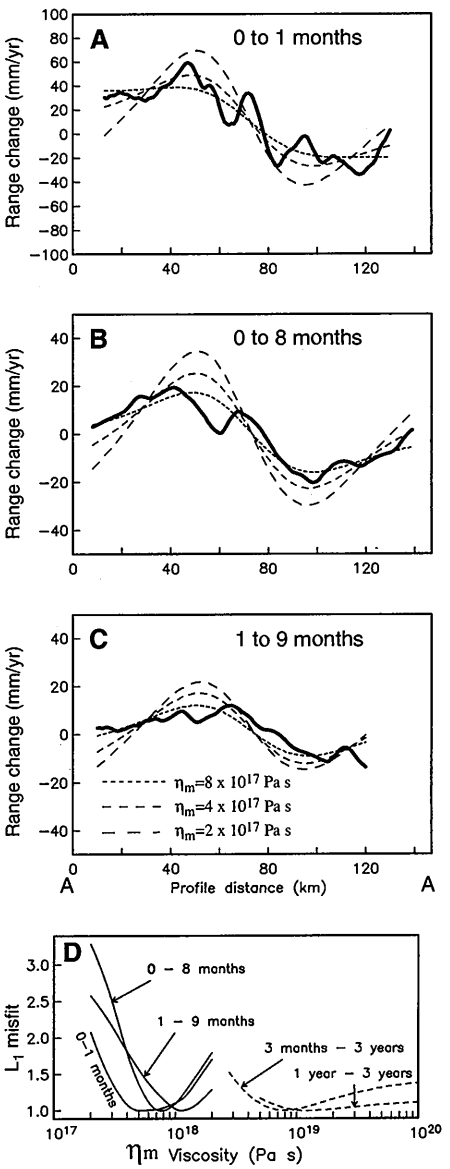

Fig. 3. Observed unwrapped range change along profile A-A′ (Fig. 1) for the time periods (**A**) 20 October 1999 to 24 November 1999 (0 to 1 month), (**B**) 20 October 1999 to 21 June 2000 (0 to 8 months), and (**C**) 24 November 1999 to 26 July 2000 (1 to 9 months). Superimposed are viscoelastic model predictions for three possible values of mantle viscosity. (**D**) Solid curves: L_1-norm misfit of observed post–Hector Mine range change along profile A-A′ with respect to the viscoelastic model as a function of η_m, with absolute minima normalized to unity. Dashed curves: misfit of observed post-Landers range change with respect to the viscoelastic model derived with interferograms from 3 months to 3 years (*16*) and 1 year to 3 years (*33*) after the Landers earthquake. In all cases, a fixed ratio of η_c/η_m = 27 is assumed.

more ductile than the lower crust (*17*). We consider a forward model with preferred values $\eta_m = \sim 4 \times 10^{17}$ Pa s and $\eta_c = 1.1 \times 10^{19}$ Pa s (Fig. 4). The calculated deformation patterns (Figs. 1D and 2B) fit the primary features of the observed postseismic range change and horizontal velocity fields. Variance reduction with respect to the InSAR data set is 67%. Fits of the postseismic model to GPS time series at representative sites (Fig. 2C) are in harmony with the exhibited time decay over the first 8 months.

Our results are consistent with the nonlinearity of upper mantle viscosity inferred from laboratory experiments of ductile olivine flow (*2*). The spatial pattern of deformation is unchanged from the earliest post–Hector Mine interval (Figs. 1 and 3), indicating that the same process is operative throughout the 9 months after the earthquake. Averaged over the first 8 months, deformation is matched best by $\eta_m \sim 3$ to 8×10^{17} Pa s. In contrast, observations from 3 months to 3 years after the 1992 Landers earthquake, 30 km to the west, require $\eta_m \sim 6$ to 8×10^{18} Pa s (*16*), an order of magnitude larger. Indeed, the Hector Mine interferograms suggest a factor of ~three increase in effective viscosity during the first 9 months after the Hector Mine earthquake, as demonstrated by the misfit patterns of the fault-parallel profiles as a function of viscosity (Fig. 3D). These and corresponding misfit patterns of two post-Landers interferograms (Fig. 3D) indicate that mantle viscosity is initially low after a large stress step, gradually increases with time, and converges to 1 to 3×10^{19} Pa s after 1 to 3 years of relaxation. Results obtained after the 1992 and 1999 earthquakes indicate stress dependence of the effective viscosity of the upper mantle.

Elsewhere in the western United States, mantle viscosity as inferred from lake drainage (*18*) and glacial unloading (*19*) sources is about 10^{19} Pa s, about the same as inferred for the 3-month to 3-year post-Landers period. The filling of Lake Mead, Nevada, about 250 km northeast of the central Mojave Desert in a similar tectonic environment, produced long-wavelength transient crustal deformation that requires the presence of a weak mantle of viscosity ~ 10^{18} Pa s (*20*). The high ductility of the sub–Mojave Desert mantle is further supported by isotopic studies (*21*, *22*) that associate young (<1 million years ago) mantle-derived basalts with an asthenospheric source between about 50- and 70-km depth.

Extrapolation of laboratory-derived flow laws suggests that Earth's continental crust should flow under lower stresses than does the uppermost mantle (*1–4*) and that the relative strength of the mantle should persist to those depths where heat transport remains predominantly conductive, about 100-km depth for a moderate geothermal gradient. However, the documented inferences of high mantle ductility throughout the western United States demand a much thinner conductive layer, and Pollitz *et al.* (*16*) pointed out that the sub-Mojave viscosity profile is consistent with an upper mantle composed of hydrous olivine with temperature between the wet and dry basalt solidus reached within the top 30 km of the mantle. Furthermore, geochemical (*23*) evidence suggests a mafic composition for the lower crust beneath the central Mojave desert, which could enhance its strength (*24*). Modeling of isostatic rebound of Lake Bonneville (*25*) and loading of Lake Mead (*20*) require a strong elastic crust about 30 km thick, consistent with our results and again suggesting behavior that is more generally applicable to the western United States.

On the other hand, other evidence supports lower crustal flow in an actively deforming continental crust. However, these processes may result from unusual thermal conditions not found in many active regions. In strongly extended crust, the requirements of isostacy (*26*) and observations of crustal imaging (*27*) strongly suggest lower crustal flow beneath metamorphic core complexes. In active mountain belts, lower crustal flow has been proposed to explain both the characteristic topography and observed partitioning among thrust, strike slip, and extensional strains (*28*, *29*). Detailed structural mapping and geochronology in a number of core complexes show that magmatism invariably precedes upper crustal extension (*30*) and proposed lower crustal flow, perhaps because of delamination of the lithospheric mantle. Such a thermal event would weaken lower crustal rocks (*31*), whereas subsequent flow and isostatic uplift would cool and restrengthen the lower crust. Lower crustal flow beneath mountain belts is documented in overthickened crust, with lower crustal rocks at more than twice their typical depths. At depths of ~50 km or more, these rocks would be at temperatures where their behavior is expected to be ductile, explaining their inferred flow in a way that is consistent with our results. Our inference of upper mantle postseismic flow suggests that during part of the seismic cycle, the lower crust acts as a stress guide coupling the upper crust to mantle motions.

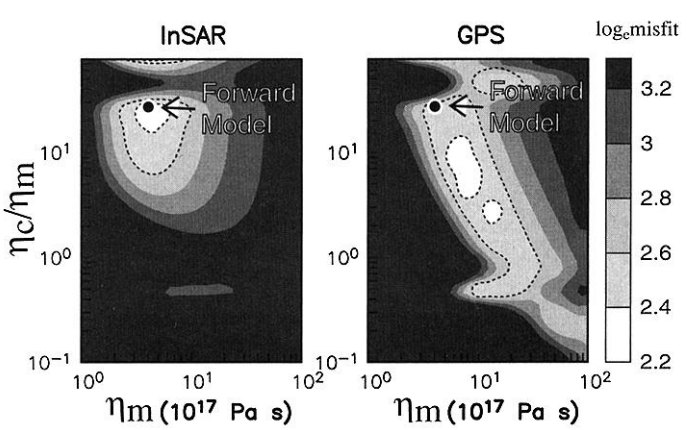

Fig. 4. Logarithmic misfit of separate InSAR (left) and GPS (right) data sets with respect to the viscoelastic deformation model (eq. 1) as a function of mantle viscosity and crust-to-mantle viscosity ratio. The viscosity combination used to generate the viscoelastic forward model calculations in Figs. 1D and 2, B and C, is indicated.

References and Notes

1. W. F. Brace, D. L. Kohlstedt, *J. Geophys. Res.* **85**, 6348 (1980).
2. S.-I. Karato, P. Wu, *Science* **260**, 771 (1993).
3. D. L. Kohlstedt, B. Evans, S. Mackwell, *J. Geophys. Res.* **100**, 17587 (1995).
4. G. Hirth, D. L Kohlstedt, *Earth Planet. Sci. Lett.* **144**, 93 (1996).
5. U.S. Geological Survey *et al.*, *Seismol. Res. Lett.* **71**, 11 (2000).
6. D. S. Dreger, A. Kaverina, *Geophys. Res. Lett.* **27**, 1941 (2000).
7. D. Massonnet, K. L. Feigl, *Rev. Geophys.* **36**, 441 (1998).
8. R. Bürgmann, P. A. Rosen, E. J. Fielding, *Annu. Rev. Earth Planet. Sci.* **28**, 169 (2000).
9. Interferograms are derived from SAR data from the European Space Agency Satellite ERS-2, made available by Institute of Geophysics and Planetary Physics, Scripps Institution of Oceanography. The image pairs were processed with precise orbital information provided by Delft University [R. Scharroo, P. N. A. M. Visser, *J. Geophys. Res.* **103**, 8113 (1998)] in conjunction with a Digital Elevation Model (DEM). Application of a boxcar filter of 1-km width and removal of the mean and trend from the original interferograms yield slightly smoothed interferograms with most of the effects of DEM and satellite orbital errors removed. During the observation periods, the satellite radar was pointed at the region at an angle of 23° from the vertical and looking from S77°E [unit vector in the range direction $\hat{l} = (0.381, -0.088, 0.921)$ in east-north-up coordinates]. Altitudes of ambiguity (*8*) are 440 m (0 to 8 months) (Fig. 1E), 43 m (1 to 9 months) (C), and −21 m (0 to 1 month) (B).
10. J. Sauber, W. Thatcher, S. C. Solomon, M. Lisowski, *Nature* **367**, 264 (1994).
11. J. C. Savage, J. L. Svarc, *J. Geophys. Res.* **102**, 7565 (1997).
12. In the afterslip model, we evaluate the static deformation on the equivalent elastic model [F. F. Pollitz, *Geophys. J. Int.* **125**, 1 (1996)] resulting from assumed right-lateral shear dislocations on vertical faults beneath the seismogenic rupture. In the viscoelastic model, we evaluate and sum the deformation resulting from lower crust and mantle relaxation after both the Landers and Hector Mine earthquakes. This viscoelastic deformation is determined by the Landers [D. J. Wald, T. H. Heaton, *Bull. Seismol. Soc. Am.* **84**, 668 (1994)] and Hector Mine (*6*) coseismic slip models in conjunction with assigned viscosities η_c and η_m [F. F. Pollitz, *J. Geophys. Res.* **102**, 17921 (1997)].
13. D. Gordon, C. Ma, J. W. Ryan, in *Contributions of Space Geodesy to Geodynamics: Crustal Dynamics*, vol. 23, D. E. Smith, Ed. (American Geophysical Union, Washington, DC, 1993), pp. 131–138.

14. Elastic upper crust and viscoelastic lower crust thicknesses are 16 km and 14 km, respectively. The assigned 16-km thickness is consistent with the cutoff depth of seismicity between about 15- and 20-km depth [K. B. Richards-Dinger, P. M. Shearer, *J. Geophys. Res.* **105**, 10939 (2000)], thought to coincide with the brittle-to-ductile transition. Depth-dependent elastic parameters are constrained by seismic information [J. Qu, T. L. Teng, J. Wang, *Bull. Seismol. Soc. Am.* **84**, 596 (1994)], and viscosities η_c and η_m are variable.
15. The 16-km upper depth is chosen to coincide with the base of the coseismic slip zone, and the 36-km depth is chosen to permit postseismic slip that is deep enough to reproduce the long-wavelength pattern of surface displacement seen on the interferograms.
16. F. F. Pollitz, G. Peltzer, R. Bürgmann, *J. Geophys. Res.* **105**, 8035 (2000).
17. We tested possible stratification within the lower crust by considering an additional model in which the lower crust consists of two uniform layers of identical thickness, with the upper layer three times as viscous as the lower layer. In this case, we found that optimal mantle viscosity is in the same range as the presented model (3 to 8 $\times$ 10^{17} Pa s), whereas the lower crustal viscosities are 1.7 $\times$ 10^{19} Pa s and 0.6 $\times$ 10^{19} Pa s. The weaker crustal layer is still much more viscous than the mantle.
18. B. G. Bills, D. R. Currey, G. A. Marshall, *J. Geophys. Res.* **99**, 22059 (1994).
19. T. S. James, J. J. Clague, K. Wang, I. Hutchinson, *Quat. Sci. Rev.* **19**, 1527 (2000).
20. G. Kaufmann, F. Amelung, *J. Geophys. Res.* **105**, 16341 (2000).
21. G. L. Farmer *et al.*, *J. Geophys. Res.* **100**, 8399 (1995).
22. B. L. Beard, C. M. Johnson, *J. Geophys. Res.* **102**, 20149 (1997).
23. A. F. Glazner *et al.*, *J. Geophys. Res.* **96**, 13673 (1991).
24. S. H. Kirby, A. K. Kronenberg, *Rev. Geophys.* **25**, 1219 (1987).
25. S. M. Nakiboglu, K. Lambeck, *J. Geophys. Res.* **88**, 10439 (1983).
26. L. Block, L. H. Royden, *Tectonics* **9**, 557 (1990).
27. J. McCarthy *et al.*, *J. Geophys. Res.* **96**, 12259 (1991).
28. L. H. Royden *et al.*, *Science* **276**, 788 (1997).
29. M. K. Clark, L. H. Royden, *Geology* **28**, 703 (2000).
30. P. B. Gans, W. A. Bohrson, *Science* **279**, 66 (1998).
31. D. McKenzie *et al.*, *J. Geophys. Res.* **105**, 11029 (2000).
32. Sixteen continuous GPS time series are provided by Southern California Integrated GPS Network (SCIGN) (http://pasadena.wr.usgs.gov/scign/cgi-bin/datafile.cgi), and 13 campaign GPS times series are provided by U.S. Geological Survey (USGS) (http://quake.usgs.gov/research/deformation/gps/auto/HectorMine) covering the time period 20 October 1999 to 21 June 2000 or a portion thereof. The SCIGN measurements are referenced to ITRF97 [C. Boucher, Z. Altamimi, P. Sillard, in *IERS Technical Note 27* (Observatoire de Paris, Paris, France, 1999)]. The USGS measurements are referenced to the SCIGN measurements by aligning the velocity fields at three common sites, achieving a consistency of about 1 mm/year between the two velocity fields.
33. D. Massonnet, W. Thatcher, H. Vadon, *Nature* **382**, 612 (1996).
34. We thank D. Sandwell, W. Prescott, J. Svarc, K. Hudnut, N. King, and S. Kirby for helpful discussions; J. Savage and R. Stein for constructive reviews; D. Dreger for providing the Hector Mine coseismic model; and G. Bawden for assistance with graphics. We acknowledge the Southern California Integrated GPS Network and its sponsors, the W. M. Keck Foundation, NASA, NSF, the U.S. Geological Survey, and the Southern California Earthquake Center, for providing GPS data used in this study. This paper benefited from constructive criticisms by two anonymous reviewers.

5 April 2001; accepted 30 July 2001

Zipf Distribution of U.S. Firm Sizes

Robert L. Axtell

Analyses of firm sizes have historically used data that included limited samples of small firms, data typically described by lognormal distributions. Using data on the entire population of tax-paying firms in the United States, I show here that the Zipf distribution characterizes firm sizes: the probability a firm is larger than size s is inversely proportional to s. These results hold for data from multiple years and for various definitions of firm size.

Firm sizes in industrial countries are highly skew, such that small numbers of large firms coexist alongside larger numbers of smaller firms. Such skewness has been robust over time, being insensitive to changes in political and regulatory environments, immune to waves of mergers and acquisitions (*1*), and unaffected by surges of new firm entry and bankruptcies. It has even survived large-scale demographic transitions within work forces (e.g., women entering the labor market in the United States) and widespread technological change. The firm size distribution within an industry indicates the degree of industrial concentration, a quantity of particular interest for antitrust policy.

Beginning with Gibrat (*2*), firm sizes have often been described by lognormal distributions. This distribution is a consequence of the "law of proportional effect," also known as Gibrat's law, whereby firm growth is treated as a random process and growth rates are independent of firm size (*3*). Such distributions are skew to the right, meaning that much of the probability mass lies to the right of the modal value. Thus, the modal firm size is smaller than the median size, which, in turn, is smaller than the mean.

The upper tail of the firm size distribution has often been described by the Yule (*1*) or Pareto (also known as power law, or scaling) distributions (*4*, *5*). For a discrete Pareto-distributed random variable, S, the tail cumulative distribution function (CDF) is

$$\Pr[S \geq s_i] = \left(\frac{s_0}{s_i}\right)^{\alpha}, \; s_i \geq s_0, \; \alpha > 0 \quad (1)$$

where s_0 is the minimum size (*6*). Recent analysis of data on the largest 500 U.S. firms gives α as $\sim$1.25, whereas it is closer to 1 for many other countries (*7*). The special case of $\alpha = 1$ is known as the Zipf distribution and has somewhat unusual properties insofar as its moments do not exist (*8*). This distribution describes surprisingly diverse natural and social phenomena, including percolation processes (*9*), immune system response (*10*), frequency of word usage (*4*), city sizes (*4*, *11*), and aspects of Internet traffic (*12*).

From an analysis using a sample of firms in Standard & Poor's COMPUSTAT, a commercially available data set, it has been reported that U.S. firm sizes are approximately lognormally distributed (*13*). The COMPUSTAT data cover nearly all publicly traded firms in the United States—some 10,776 firms in 1997, almost 4300 of which had more than 500 employees. Firms covered by COMPUSTAT collectively employed over 52 million people, approximately one-half of the U.S. work force. However, these data are unrepresentative of the overall population of U.S. firms. Data from the U.S. Census Bureau put the total number of firms that had employees sometime during 1997 at about 5.5 million, including over 16,000 having more than 500 employees. Furthermore, the Census data have a qualitatively different character than the COMPUSTAT data. Census data display monotonically increasing numbers of progressively smaller firms, a shape the lognormal distribution cannot reproduce, and suggesting that a power law distribution may apply. As shown in Table 1 (*14*), the mean firm size in the COMPUSTAT data is 4605 employees (6349 for firms larger than 0), whereas in the Census data it is

Table 1. U.S. firm size distribution in 1997, compared across data sources. Number of firms in various size categories, with size defined as the number of employees, comparing COMPUSTAT and U.S. Census Bureau data for 1997. Note that there are monotonically decreasing numbers of progressively larger firms in the Census data, whereas this is not the case in the COMPUSTAT data (*29*).

Size class	COMPUSTAT	Census
0	2,576	719,978
1 to 4	123	2,638,070
5 to 9	149	1,006,897
10 to 19	251	593,696
20 to 99	1,287	487,491
100 to 499	2,123	79,707
500+	4,267	16,079
Total	10,776	5,541,918

Center on Social and Economic Dynamics, The Brookings Institution, 1775 Massachusetts Avenue, NW, Washington, DC 20036, USA.

Correspondence should be addressed to raxtell@brookings.edu.